Tellus SERIES A DYNAMIC METEOROLOGY AND OCEANOGRAPHY
PUBLISHED BY THE INTERNATIONAL METEOROLOGICAL INSTITUTE IN STOCKHOLM

Tellus (2008), 60A, 749–760
Printed in Singapore. All rights reserved

TELLUS

Scaling of the Atlantic meridional overturning circulation in a global ocean model

By HENK A. DIJKSTRA*, *Institute for Marine and Atmospheric Research Utrecht, Department of Physics and Astronomy, Utrecht University, Princetonplein 5, 3584 Utrecht, the Netherlands*

(Manuscript received 13 March 2007; in final form 25 February 2008)

ABSTRACT

Using a global ocean model, we revisit the issue of the scaling of the Atlantic Meridional Overturning Circulation (AMOC) versus the vertical diffusivity. With a continuation approach, we are able to compute curves of exact steady solutions of the global model versus the magnitude of the vertical diffusivity K_V in the model; we find that the AMOC strength scales as $K_V^{1/3}$. This result is analysed with help of the local density balances in the Atlantic and Pacific. It appears that processes in the Pacific are crucial for the scaling behaviour of the AMOC.

1. Introduction

There has been quite some discussion in literature on the issue of the dependence of the strength of the Atlantic Meridional Overturning Circulation (AMOC) on forcing conditions and representations of internal processes such as vertical mixing (Gnanadesikan, 1999; Park and Bryan, 2000, 2001; Klinger et al., 2003; Levermann and Griesel, 2004; Dalan et al., 2005; Lucas et al., 2006). An adequate answer is important since it will lead to an understanding of the processes controlling the AMOC and the sensitivity of the associated heat transport to changes in external forcing conditions.

The classical view of the scaling behaviour between MOC and vertical diffusivity started with work on buoyancy-driven flows in a single-hemispherical basin, representing the North Atlantic (Lineikin, 1955; Robinson and Stommel, 1959; Bryan and Cox, 1967). In case of restoring surface conditions and a linear equation of state, there is effectively one tracer, and the description of the flow in either density or temperature is equivalent. Assuming that the flow is geostrophic and hydrostatic and that an upwelling-diffusion balance controls the depth of the thermocline, the classical scaling relations are

$$V = \frac{g\alpha_T \Delta T \delta_T}{fL}; \quad \delta_T = \left(\frac{K_V L^2 f}{g\alpha_T \Delta T}\right)^{1/3};$$
$$\psi_A = V\delta_T L = \left(\frac{K_V^2 L^4 g\alpha_T \Delta T}{f}\right)^{1/3}. \quad (1)$$

Here ψ_A is the strength of the MOC, f a characteristic value of the Coriolis parameter, K_V the vertical diffusivity, L a characteristic horizontal length scale, V a characteristic horizontal velocity scale, α_T the thermal compressibility, g the acceleration due to gravity and ΔT the equator-to-pole temperature difference. The quantity δ_T is a measure of the thermocline depth, often computed as the depth where the temperature has decreased by some factor of the total vertical temperature difference. The crucial element of the scaling eq. (1) is that a change in K_V changes the thermocline depth δ_T, and the strength of the horizontal flow patterns follow this scale through self-similarity. The vertical velocity scale W is determined by the advection–diffusion balance ($W = K_V/\delta_T$) in the temperature equation. When wind forcing is present, the Ekman pump velocity can also be a scale controlling the vertical velocity (Welander, 1986). The thermocline scale can then be advectively controlled, that is, no effect of diffusion, in which case the strength of the MOC is independent of the vertical diffusivity K_V.

With the availability of ocean models, scaling relations can be tested with numerical equilibrium solutions. For the single-hemispherical case, the scaling of the MOC with K_V has been clarified (Park and Bryan, 2000, 2001) using both a z-coordinate model (MOM) and an isopycnal model (HIM). In this case, the scaling without wind is according to (1), independent of the type of model. Deviations from this scaling found in earlier studies (Bryan, 1987; Colin de Verdière, 1988; Hu, 1996; Marotzke and Scott, 1997) could be explained by the following factors: (i) the dependence of the surface temperature on K_V under restoring conditions with a non-zero restoring time scale and (ii) the evaluation of the meridional overturning streamfunction using density or depth as vertical coordinate.

*Correspondence.
e-mail: dijkstra@phys.uu.nl
DOI: 10.1111/j.1600-0870.2008.00326.x

A significant extension of the classical scaling behaviour was presented in Gnanadesikan (1999). In addition to the processes above, the Ekman transport induced by Southern Ocean winds and the mixing effects due to Southern Ocean eddies were considered. From continuity of the transport in a double-hemispherical basin with a southern channel, Gnanadesikan (1999) finds a cubic equation for the characteristic thermocline depth ($d\delta_T$), which can be written (Klinger et al., 2003) as

$$d^3 + Sd^2 - Ed - 1 = 0, \tag{2}$$

where the dimensionless parameters S and E are given by

$$E = \frac{\tau_s L_s \delta_{Ta}}{\rho_0 f_s K_V A}; \quad S = \frac{L_s A_I}{A L_y K_V \delta_{Ta}^2}. \tag{3}$$

Here L_s is the zonal dimension of the southern channel, f_s and τ_s are the mean Coriolis parameter and zonal wind stress, respectively, in the channel, A is the surface of upwelling in the Atlantic basin, A_I represents the mixing effect due to Southern Ocean eddies, ρ_0 is a reference density and L_y is a characteristic meridional length scale in the Atlantic basin, where the thermocline depth is non-zero. When the Southern Ocean winds are not considered ($E = 0$) and the effect of eddy mixing can be neglected ($S = 0$), then there is only one solution ($d = 1$), which leads to the classical scaling eq. (1). Regimes of flow as predicted by eq. (2) have been shown to occur in a z-coordinate and an isopycnal ocean general circulation model (OGCM) for this configuration (Klinger et al., 2003). Again, the scaling according to solutions of (2) assumes self-similarity of the horizontal fields. In addition, it is assumed that different processes contribute to the transport through the same thermocline scale.

Recently, the results in the Gnanadesikan (1999) paper have been criticized by Levermann and Griesel (2004), who show that there are only two solutions to eq. (2) which exhibit a proper scaling behaviour between the meridional pressure difference Δp and the strength ψ_A of the MOC. In the classical situation, with prescribed surface density, $\psi_A \sim (\Delta p)^{\frac{1}{2}}$ and this case corresponds to all upwelling at low latitudes (the single-hemispherical case), which is unrealistic. The other case is that of a linear scaling $\psi_A \sim \Delta p$, but this corresponds to a localized flow in the Southern Ocean where all the downward volume transport is due to the eddy-induced return flow, also an unrealistic situation to Levermann and Griesel (2004). They present results from an EMIC, the Climber-3α model, that display a linear relationship between ψ_A and Δp. The Atlantic thermocline depth does not change when the meridional density gradient is changed, in correspondence with earlier GCM results (Rahmstorf, 1996).

Using an idealized two-basin configuration, Furue and Endoh (2005) provide indications that changing the amplitude and vertical distribution of the vertical diffusivity in the Pacific affects the strength of the AMOC. When the vertical diffusivity is weakened in the Pacific, the strength of the AMOC is also reduced. Although they mention a linear relationship between global deep overturning and K_V, they have computed only a few equilibrium solutions and hence are not able to determine specific scaling relations. The scaling behaviour of the MOC was studied in such a two-basin configuration by Dalan et al. (2005) using an idealized coupled ocean-atmosphere model. They find the interesting result that the AMOC scales with a power 0.44 of K_V but that the Southern Pacific MOC scales with a power of 0.63. This result in Dalan et al. (2005) is based on only four equilibrium solutions. Such computations are indeed expensive as it takes a long time to integrate a global model to equilibrium for small values of K_V.

With fully-implicit ocean models, the issue becomes computationally much more efficient. In Weijer et al. (2003), we presented results on a scaling of the AMOC strength ψ_A versus K_V within a global GCM, and it was found that $\psi_A \sim K_V^{1/3}$, but the physics of this relationship was never explored in detail. Bifurcation diagrams of this model with the strength of the freshwater input in the northern North Atlantic as control parameter were presented in Dijkstra and Weijer (2005) and showed good qualitative agreement with those in traditional OGCMs (Rahmstorf, 2000). The multiple equilibrium regime is caused by the salt-advection feedback, and it is associated with a the occurrence of two saddle-node bifurcations. However, the scaling relations between the AMOC and the meridional pressure (or density) difference (as in Levermann and Griesel, 2004) were not further explored in Dijkstra and Weijer (2005).

The great advantage of the fully implicit global ocean model is that exact steady-states can be determined versus parameters using continuation methods (Dijkstra, 2005). We will use this approach here to study the scaling behaviour of the strength of the AMOC versus K_V, both under (Levitus-) restoring conditions and mixed boundary conditions. After a brief description in Section 2 of the model and methods used, it is shown in Section 3 that under restoring conditions for surface salinity the scaling exponents of the Atlantic, Pacific and global MOC with K_V are 1/3, 2/3 and 2/3, respectively. In addition, under mixed boundary conditions, a linear relation between the meridional pressure (or density) difference in the Atlantic and the AMOC is found, as in Levermann and Griesel (2004). The aim of the analysis of these results in Section 4 is to provide a context that explains apparent discrepancies between earlier results (Gnanadesikan, 1999; Levermann and Griesel, 2004). Central in this analysis is the fact that processes in the Pacific are important for setting the strength of the AMOC.

2. Formulation

In this section, we will shortly recall the fully implicit ocean model used (Section 2.1) and briefly describe the continuation methods which are applied to this model to compute bifurcation diagrams and scaling relations (Section 2.2).

2.1. Model

The description of the fully-implicit global ocean model used in this study is presented in Weijer et al. (2003) and Dijkstra and Weijer (2005), to which the reader is referred for full details. The governing equations of the ocean model are the hydrostatic, primitive equations in spherical coordinates on a domain that includes full continental geometry as well as bottom topography. The ocean velocities in east- and northward directions are indicated by u and v, the vertical velocity is indicated by w, the pressure by p and the temperature and salinity by T and S, respectively.

Vertical and horizontal mixing of momentum and heat/salt are represented by a Laplacian formulation with prescribed eddy viscosities A_H and A_V and eddy diffusivities K_H and K_V, respectively. Compared with the Gnanadesikan (1999) model, we represent the 'eddy' effects here only by horizontal (downgradient) diffusion. As it is not easy to include more sophisticated mixing parameterizations such as Gent and McWilliams and neutral physics in these implicit models (one needs to compute explicit Jacobian matrices of these operators), the effect of more realistic mixing representations is outside the scope of this paper. We will use depth dependent values of K_H and K_V according to (Bryan and Lewis, 1979; England, 1993)

$$K_V(z) = \kappa K_V^0 \left[1 - \eta_s \arctan \mu(z - z_*)\right], \tag{4a}$$

$$K_H(z) = K_H^0 + \left(A_r - K_H^0\right) e^{\frac{z}{500}}, \tag{4b}$$

with $z \in [-5000, 0]$). Here, $K_H^0 = 0.5 \times 10^3\,\mathrm{m^2s^{-1}}$, $A_r = 1.0 \times 10^3\,\mathrm{m^2s^{-1}}$, $K_V^0 = 8.0 \times 10^{-5}\,\mathrm{m^2s^{-1}}$, $\eta_s = 0.41$, $\mu = 4.5 \times 10^{-3}\,\mathrm{m^{-1}}$, $z_* = -2.5 \times 10^3$ m and κ is a parameter, which will be varied later on. The spatial patterns of both $K_V(z)$ and $K_V(z)$ are shown versus z for $\kappa = 1$ in Fig. 1. The vertical diffusivity K_V increases from $3.1 \times 10^{-5}\,\mathrm{m^2s^{-1}}$ at the surface to $1.3 \times 10^{-4}\,\mathrm{m^2s^{-1}}$ near the bottom of the flow domain. The horizontal diffusivity increases monotonically from $5.0 \times 10^2\,\mathrm{m^2\,s^{-1}}$ at the bottom of the ocean to $10^3\,\mathrm{m^2\,s^{-1}}$ near the surface.

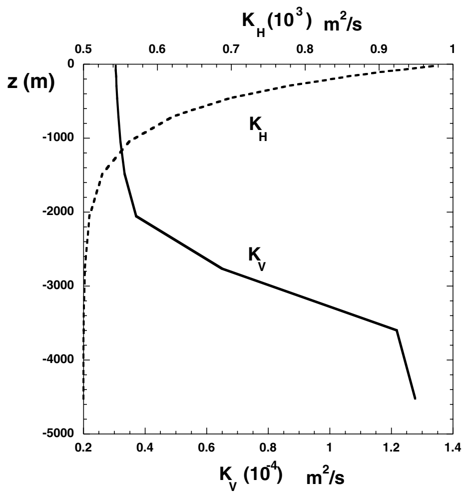

Fig. 1. Vertical dependence of the diffusivities K_V (lower x-axis) and K_H (upper x-axis) as in (4) for $\kappa = 1.0$.

The oceanic flow is forced by the annual mean wind stress as given in Trenberth et al. (1989). The upper ocean is coupled to a simple energy-balance atmospheric model (Dijkstra and Weijer, 2005) in which only the heat transport is modelled (no moisture transport). Either restoring conditions for the salinity or prescribed freshwater fluxes are used in the results below. As in low-resolution OGCMs, the surface forcing is represented as a body forcing over the upper layer. On the continental boundaries, no-slip conditions are prescribed and the heat- and salt fluxes are zero. At the bottom of the ocean, both the heat- and salt fluxes vanish and slip conditions are assumed.

2.2. Methods

The horizontal resolution of the global model is about 4° (a 96 × 38 Arakawa C-grid on the domain [180°W, 180°E] × [85.5°S, 85.5°N]) and the grid has 12 levels in the vertical. The vertical grid is non-equidistant with the most upper (lowest) layer having a thickness of 50 m (1000 m). We determine steady-state solutions versus parameters using continuation methods (Dijkstra, 2005). The discretized steady equations can be written as a non-linear algebraic system of equations of the form

$$\mathbf{F}(\mathbf{x}, \lambda) = 0, \tag{5}$$

where $\mathbf{x}$ is the state vector (containing u, v, w, p, T and S at the gridpoints) and λ is a control parameter. For the global ocean model with the resolution as above, the dimension of the state space (and of $\mathbf{x}$) is 284 544.

To compute a branch of stationary solutions in a control parameter, say λ, a pseudo-arclength method is used (Keller, 1977). The branches of stationary solutions $(\mathbf{u}(s), \lambda(s))$ are parameterized by an arclength parameter s. Since this introduces an extra unknown, an additional equation is needed. To obtain this equation the tangent is normalized along the branch giving the result

$$\dot{\mathbf{x}}_0^T(\mathbf{x} - \mathbf{x}_0) + \dot{\lambda}_0^T(\lambda - \lambda_0) - \Delta s = 0, \tag{6}$$

where Δs is the step length, the superscript^T denotes the transpose, a dot indicates differentiation with respect to s and $\mathbf{x}_0$ indicates a previous solution computed for $\lambda = \lambda_0$. The Newton–Raphson method is used to converge to the branch of stationary solutions. This method finds isolated steady solutions regardless of their stability. The linear systems arising from the Newton–Raphson method are solved with an iterative linear systems solver using a specific preconditioning technique (Dijkstra et al., 2001).

3. Results

Under restoring conditions for the surface salinity field (Levitus, 1994), a steady solution is determined for 'most realistic' values of the parameters (see Dijkstra and Weijer, 2005) of the model. The steady-state is referred below to as the reference state. We consider two cases: a restoring case in which the surface salinity field is approximately prescribed, which is akin to the approach in Gnanadesikan (1999) and a mixed case where the freshwater flux is prescribed, which follows the approach in Levermann and Griesel (2004) in the Climber-3α model.

3.1. Restoring case

In this case, the surface salinity field is strongly restored to prescribed values (Dijkstra and Weijer, 2005), and steady-states are determined versus the parameter κ in eq. (4a). As indicators of the solutions, we monitor ψ_A as the positive maximum of the Atlantic meridional overturning streamfunction, and ψ_P, ψ_G as the absolute value of the negative minimum of the Pacific and global meridional overturning streamfunction, respectively. In this way, we monitor the maximum northern overturning in the Atlantic and the maximum southern overturning of the Pacific and global overturning flow field.

The plot of ψ_A versus $K = \kappa K_V^0$ (dots in Fig. 2a) clearly indicates that there is a 1/3 power dependence. Both ψ_P (squares in Fig. 2a) and ψ_G versus K (diamonds in Fig. 2a), however, follow a 2/3 power scaling only for relatively large values of K, and both have a weak dependence on K at small diffusivity values. As the wind-driven surface signal is also contained in the maximum values, we also the plot the maximum meridional overturning streamfunction values below 250 m in Fig. 2b. This hardly has any effect on the Atlantic values as maxima occur below 250 m, but for the Pacific and global MOC, one now clearly sees the 2/3 power-law scaling. In Fig. 2c, the maximum value of ψ_A is plotted over vertical sections at 20°S, 10°N and 40°N, the latter having approximately the value of the maximum overturning. From this figure we see that the exponent is slightly less than 1/3 in the tropical Atlantic and South Atlantic. The meridional heat transport Φ_H at 20°N is plotted versus the maximum overturning in the Atlantic in Fig. 2d, showing a near-linear relation as expected.

Contour plots of the Atlantic MOC for several values of K are shown in Fig. 3, with specific values of K and the corresponding values of ψ_A indicated in the caption. As K increases, there are two significant changes in the flow pattern. First, more and more upwelling occurs north of the southern boundary of the Atlantic (at 35°S). While closed streamlines appear only north of 10°S at small K (Fig. 3a), they occur over the whole domain in Fig. 3d. In Fig. 3a, 6 Sv of the 9 Sv sinking leaves the Atlantic in the lowest 3 km. On the contrary, about 12 Sv of the 23 Sv sinking leaves the 30°S boundary in Fig. 3d. A second feature is that the location of maximum overturning shifts to slightly larger depths as K increases.

At small K values, the Pacific meridional overturning appears dominated by the wind-driven surface component and the Pacific MOC is relatively weak below 1000 m (Fig. 4a). With increasing K, we see the southern cell developing (Figs. 4b and c) and at the highest value of K used, the southern cell has strongly increased in strength (Fig. 4d). Also in the Pacific MOC, one sees that the maximum values of the MOC occur at slightly larger depths as K is increased.

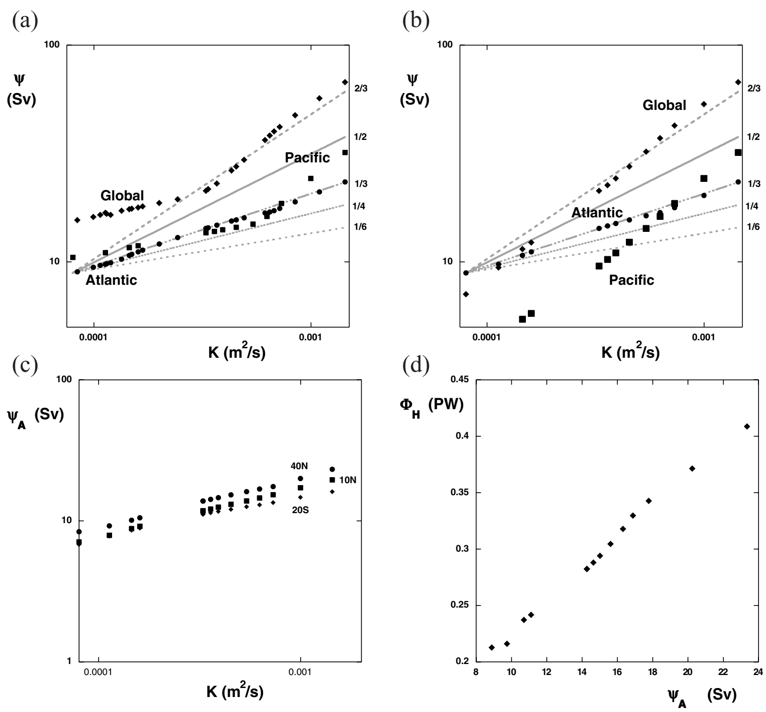

Fig. 2. (a) Scaling of the strength of the Atlantic MOC (solid dots), the Pacific MOC (solid squares) and the global MOC (solid diamonds) versus $K = \kappa K_V^0$. Each dot represents a steady-state solution; the lines are power-law dependence, which all start at the reference solution for $\kappa = 1$, that is, at $K = K_V^0$ where $K_V(z)$ is as in Fig. 1. (b) Same as (a), but now the extreme values of the MOC are calculated in the domain below 250 m. (c) Dependence of the maximum of ψ_A along a vertical section at the latitudes indicated (20°S, 10°N and 40°N) on $K = \kappa K_V^0$. (d) Relation between the meridional heat transport at 20°N in the Atlantic and the maximum meridional overturning ψ_A.

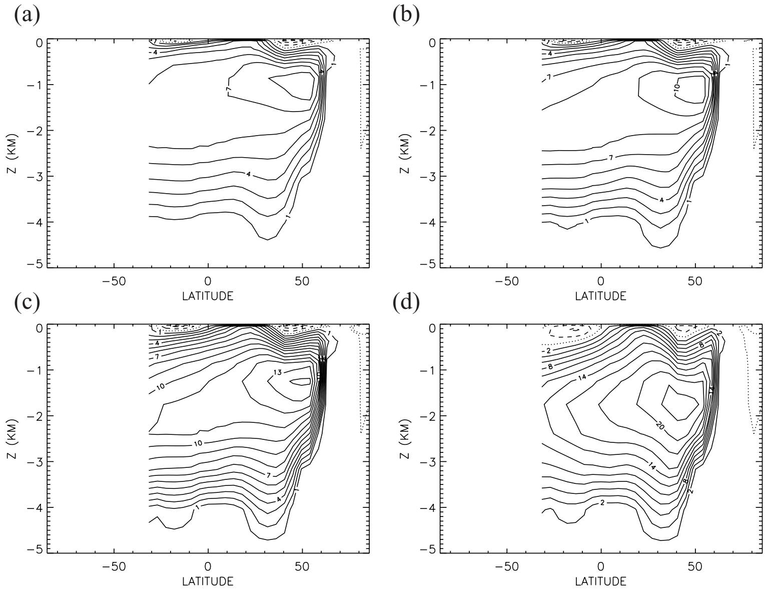

Fig. 3. Contour plots of the Atlantic meridional overturning streamfunction for different values of $K = \kappa\, K_V^0$. Contour values are in Sv. (a) $K = 8.0 \times 10^{-5}$ m^{2}s^{-1}, $\psi_A = 8.9$ Sv; (b) $K = 1.5 \times 10^{-4}$ m^{2}s^{-1}, $\psi_A = 10.7$ Sv; (c) $K = 3.3 \times 10^{-4}$ m^{2}s^{-1}, $\psi_A = 14.3$ Sv and (d) $K = 1.4 \times 10^{-3}$ m^{2}s^{-1}, $\psi_A = 23.3$ Sv.

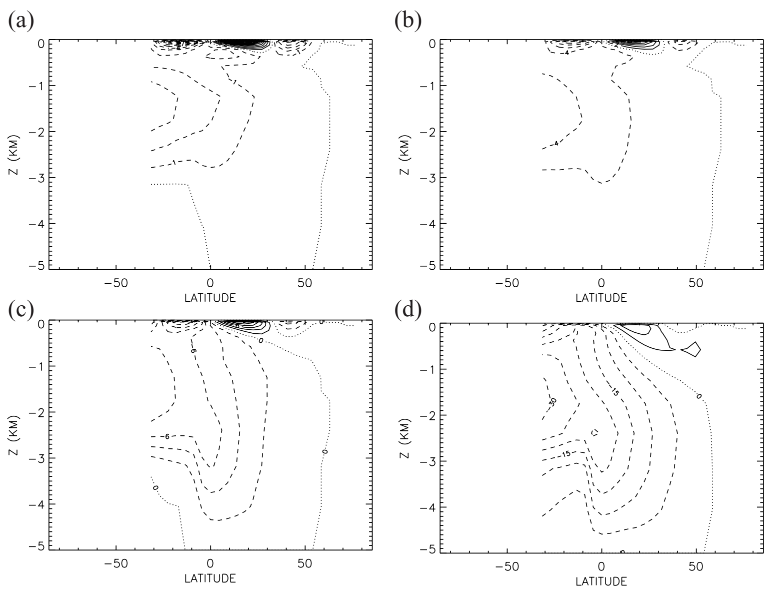

Fig. 4. Contour plots of the Pacific meridional overturning streamfunction for different values of $K = \kappa\, K_V^0$. Contour values are in Sv. (a) $K = 8.0 \times 10^{-5}$ m^{2}s^{-1}, $\psi_P = 10.5$ Sv; (b) $K = 1.5 \times 10^{-4}$ m^{2}s^{-1}, $\psi_P = 11.6$ Sv; (c) $K = 3.3 \times 10^{-4}$ m^{2}s^{-1}, $\psi_P = 13.6$ Sv and (d) $K = 1.4 \times 10^{-3}$ m^{2}s^{-1}, $\psi_P = 31.9$ Sv.

3.2. Mixed case

In the mixed case, we consider the impact of a localized freshwater flux perturbation with strength γ_p on the steady-state flows under prescribed freshwater flux conditions. As in Dijkstra and Weijer (2005), the procedure to compute steady solutions versus γ_p is the following:

(i) From the reference steady solution the freshwater flux, say F_S^e, is diagnosed.
(ii) An anomalous freshwater flux F_S^p over a region near New Foundland with domain $(\phi, \theta) \in [60°W, 24°W] \times [54°N, 66°N]$ is prescribed with strength γ_p Sv. If $F_S^p = 1$ in this domain and zero outside, then the total freshwater flux is prescribed as

$$F_S = F_S^e + \gamma_p F_S^p - Q, \tag{7}$$

where the quantity Q is determined such that

$$\int_{S_{oa}} F_S\, r_0^2 \cos\theta \,\mathrm{d}\theta\, \mathrm{d}\phi = 0. \tag{8}$$

Here, S_{oa} is the ocean-atmosphere surface.
(iii) We determine the branch of steady solutions versus γ_p, starting from the reference solution determined for $\gamma_p = 0$.

Because the reference solution for $\kappa = 1$ (Fig. 3a) has a weak AMOC ($\psi_A = 8.9$ Sv), we take as unperturbed solution the one for $\kappa = 4.1$ (with the AMOC in Fig. 3c having $\psi_A = 14.3$ Sv). We diagnose the freshwater flux of this solution and then add the

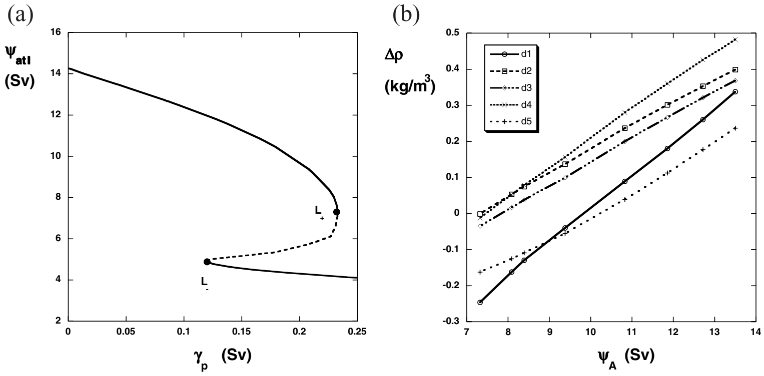

Fig. 5. (a) Bifurcation diagram as a plot of the positive maximum of the Atlantic meridional overturning streamfunction ψ_A versus γ_p for the case $\kappa = 4.1$ in (4a); a solid (dashed) line indicates (un)stable steady-states. (b) Strength of the Atlantic MOC versus the meridional density difference $\Delta\rho$ as computed in eq. (9). The different cases d_i, $i = 1, 2, 3, 4$ indicate different integration depths and latitudinal boundaries used in eq. (9), with d_1: $\theta_s = 35°$S, $\theta_n = 60°$N, $z_b = -300$ m, $z_t = -20$ m; d_2: $\theta_s = 35°$S, $\theta_n = 60°$N, $z_b = -1000$ m, $z_t = -20$ m; d_3: $\theta_s = 30°$S, $\theta_n = 60°$N, $z_b = -1000$ m, $z_t = -20$ m; d_4: $\theta_s = 35°$S, $\theta_n = 70°$N, $z_b = -1000$ m, $z_t = -20$ m. d_5: $\theta_s = 10°$N, $\theta_n = 60°$N, $z_b = -1000$ m, $z_t = -20$ m.

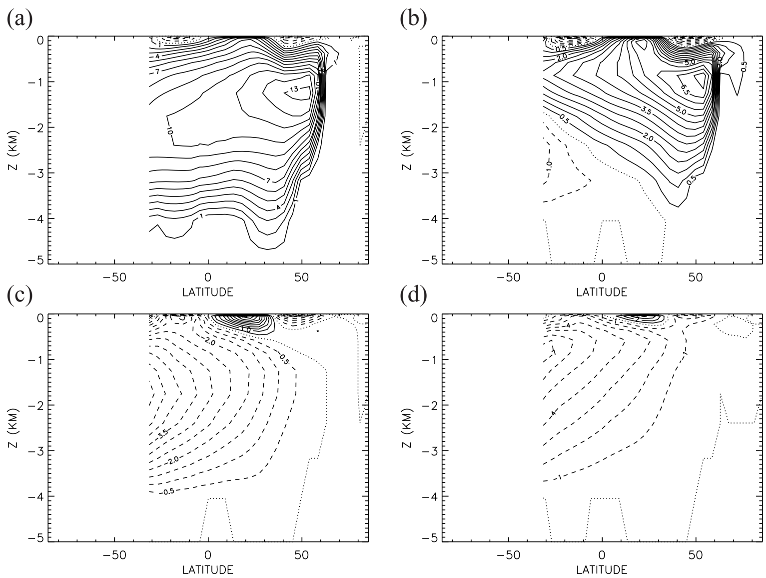

Fig. 6. Contour plot of the Atlantic MOC for several values of γ_p along the bifurcation diagram in Fig. 5a. Contour values are in Sv. (a) $\gamma_p = 0.042$ Sv, $\psi_A = 13.5$ Sv. (b) $\gamma_p = 0.23$ Sv, $\psi_A = 7.3$ Sv. (c) $\gamma_p = 0.12$ Sv, $\psi_A = 4.9$ Sv. (d) $\gamma_p = 0.23$ Sv, $\psi_A = 4.2$ Sv.

freshwater perturbation. The bifurcation diagram in which ψ_A is plotted versus γ_p is shown in Fig. 5a. The bifurcation diagram shows the typical back-to-back saddle-node bifurcations L_- and L_+, which bound the multiple equilibria regime. Values of γ_p at L_- and L_+ are given by $\gamma_p^- = 0.120$ Sv and $\gamma_p^+ = 0.232$ Sv, respectively. Note that, although the plotted bifurcation diagram depends on the norm of the solution (here ψ_A), the values of γ_p at the saddle-node bifurcations are independent of the norm chosen.

Solutions of the AMOC along several points of the curve in Fig. 5a are plotted in Fig. 6. For small γ_p, the solution of the AMOC is near to the reference state with strong northern sinking and no bottom water of southern origin (Fig. 6a). Along the bifurcation diagram, the strength of the AMOC decreases with increasing γ_p until the saddle-node bifurcation at L_+ (Fig. 5a). In the pattern of the AMOC, the return flow shallows (Fig. 6b) and the deep flow from the south strengthens. Once on the unstable branch of steady-states from L_+ to L_-, this southern sinking component increases (Fig. 6c), leading eventually to the stable collapsed state (Fig. 6d) for values of γ_p on the stable bottom branch (Fig. 5a). It can also be seen that although Antarctic Bottom Water is absent in the reference solution, it can be present in this model under slightly different freshwater flux conditions.

As in Rahmstorf (1996), we determine an indicator of the meridional density difference $\Delta\rho$ as

$$\Delta\rho = \frac{1}{A}\int_{z_b}^{z_t} [\bar{\rho}(\theta_n, z) - \bar{\rho}(\theta_s, z)]\,\mathrm{d}z \tag{9}$$

where the bar indicates zonal averaging, z_t and z_b indicate the depth range over which vertical integration is performed and A is the surface of the section over which integration is done, with θ_s and θ_n as latitudinal boundaries. In Fig. 5b, we plot $\Delta\rho$ for several choices of the four quantities z_t, z_b, θ_s and θ_n. In each case, there is a near-linear relation between $\Delta\rho$ and ψ_A in this global model. As the meridional pressure difference is linearly related to the meridional density difference also, a linear relation is found between the pressure difference in the North Atlantic (case d5 in Fig. 5b) and the AMOC strength similar to the results in Levermann and Griesel (2004).

As shown in Weijer et al. (2003), when the same model is configured for a single-hemispherical idealized Atlantic case, there is a $K_V^{2/3}$ behaviour of ψ_A in correspondence with the classical scaling. From this result in Weijer et al. (2003) and the ones in this section, we see that our model is able to provide (i) a classical 2/3 power-law relation in the single-hemispherical basin under restoring conditions, (ii) a linear relation between $\Delta\rho$ and ψ_A under mixed boundary conditions as in the Levermann and Griesel (2004) EMIC results and (iii) a 2/3 power-law behaviour of ψ_P and ψ_G versus K in the global model under restoring conditions as in the classical case, but (iv) with a 1/3 power-law behaviour of ψ_A versus K. In the next section, we provide a further analysis within the present model context to find a framework consistent with all these results.

4. Analysis

As we know from classical theory, the balances in the density equation are crucial. From the difference between the Pacific overturning streamfunction and the Atlantic overturning streamfunction in Figs. 3 and 4, we conclude that most of the upwelling occurs in the Pacific Ocean. We therefore analyse first the Pacific, then the southern connection between the Atlantic and the Pacific and finally, the Atlantic.

4.1. Processes in the Pacific

In the Pacific, there is upwelling north of 30°S, and we choose a representative location Q_P at (180°W, 25°N). Density profiles for several values of K (Fig. 7a) indicate that there is a reasonable pycnocline structure. The vertical density gradients decrease with increasing K, as expected, and 'by eye' one can see that the pycnocline depth increases; a typical pycnocline depth is about 1000 m. We calculate a measure of this depth, say δ_ρ, as the depth where

$$\rho(z = -\delta_\rho) = \rho_t + \eta(\rho_b - \rho_t), \tag{10}$$

where ρ_t is taken at $z_t = -100$ m, ρ_b at $z_b = -4500$ m and η is a constant. The pycnocline depth here measures the depth at which the density has increased by a fraction η of the total vertical difference. The area integrated value δ_P (bounded by a 20° section in longitude and 10° section in latitude centred around Q_P) is plotted as a function of K for three different values of η in Fig. 7b. Although there is a dependence of the specific value of δ_P on η, all the curves have a similar shape. The curves are not straight lines but approach a 1/3 power scaling (solid line) at relatively large values of K. At smaller values of K, the wind forcing likely contributes to the vertical velocity scale and hence the dependence of δ_P on K is weaker.

At the location Q_P, we next consider the balances in the density equation for two values of K (Fig. 8). The curve labeled **check** is the net residue in the density balance. The balance is accurate to 0.1% with respect to the largest terms in the equation, which is a consequence of the fact that we compute exact (up to numerical accuracy) steady-states. In the upper 500 m, about every term contributes to the density balance, in particular, the horizontal advection and diffusion terms. Below 500 m, the pycnocline region, there is a clear dominant balance between vertical advection and vertical diffusion. It appears that in the Pacific, the δ_P scaling is set just by the classical theory, and this very likely explains its 1/3 power-law dependence at large K.

According to the results above, the Pacific may be a central element in the scaling of the Atlantic MOC versus K as suggested already in Dalan et al. (2005). This motivates to extend the classical model to include at least two basins (Fig. 9a). In the Pacific, we know from the model results that the pycnocline thickness δ_P scales with $K^{1/3}$ as follows from the geostrophic, hydrostatic (or Sverdrup) balances together with an advection–diffusion balance in upwelling areas. According to the classical scaling, the characteristic meridional velocity V_P scales with δ_P.

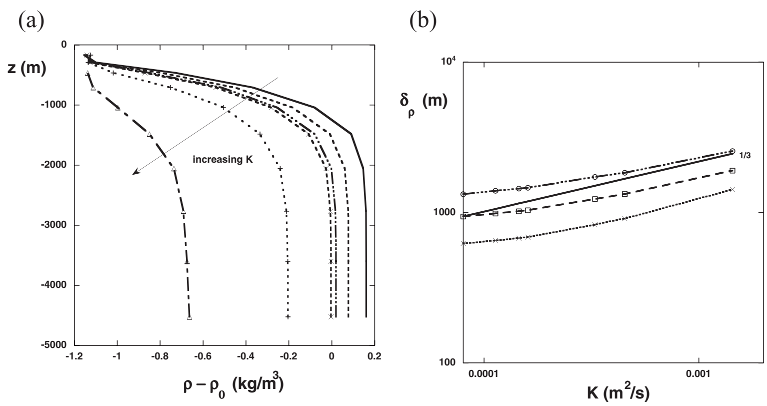

Fig. 7. (a) Profiles of $\rho - \rho_0$ in the North Pacific at the location Q_P at (180°W, 25°N) for different values of $K = \kappa K_V^0$ with: $\kappa = 1.0$ (solid); $\kappa = 1.41$ (dashed); $\kappa = 1.82$ (dashed-dotted); $\kappa = 2.0$ (dashed-crosses); $\kappa = 4.1$ (dotted-plusses) and $\kappa = 5.6$ (dashed-dotted-triangles). (b) Dependence of the area mean pycnocline depth δ_P in eq. (10) on K for $\eta = 0.9$ (dashed-dotted), $\eta = 0.75$ (dashed) and $\eta = 0.5$ (dotted). The drawn line is a power-law scaling with exponent 1/3.

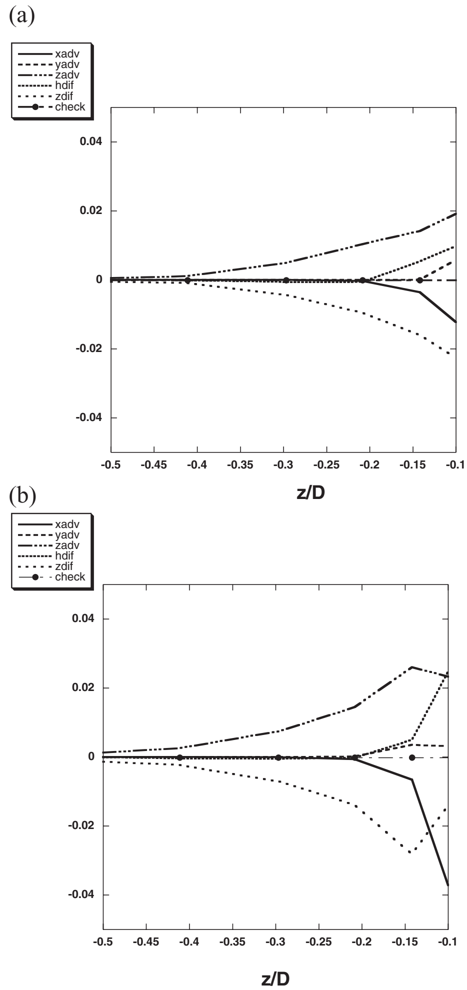

Fig. 8. Terms in the density equation for two values of K in the North Pacific at the location Q_P (25°N, 180°W) over a range of z/D where $D = 5000$ m. The different terms are indicated on the y-axis, with **xadv**: zonal advection, **yadv**: meridional advection, **zadv**: vertical advection, **hdif**: horizontal diffusion, **zdif**: vertical diffusion and **check** is the net residue in the density equation. (a) $K = 8.0 \times 10^{-5}\,\mathrm{m^2s^{-1}}$. (b) $K = 1.5 \times 10^{-4}\,\mathrm{m^2s^{-1}}$.

4.2. Southern connection

The main question now is: What is the connection of the meridional velocity scales in the Atlantic and Pacific? To investigate this, we first plot the zonal mean meridional velocity $\langle v_A\rangle(\theta_s, z)$ in the Atlantic (Fig. 9b) and $\langle v_P\rangle$ (θ_s, z) in the Pacific (Fig. 9c), both at $\theta_s = 35°$S. With increasing K, the surface negative (positive) meridional velocities increase in the Pacific (Atlantic), whereas at the bottom flow, just the opposite occurs. In the southern channel, the zonal momentum balance is given by

$$-fv = -\frac{1}{\rho_0 r_0 \cos\theta}\frac{\partial p}{\partial \phi} + A_V \frac{\partial^2 u}{\partial z^2} + \mathcal{F}^{\phi} \qquad (11)$$

where $\mathcal{F}^{\phi}$ represents horizontal mixing of momentum, A_V is the vertical viscosity and $f = 2\Omega \sin\theta$ is the Coriolis parameter. When eq. (11) is integrated over an unblocked latitude circle in the channel and over a depth range between the top of bottom topography and the Ekman layer (where friction can be neglected), we find (Warren et al., 1997; Olbers, 1998)

$$\int_0^{2\pi}\int_{z_b}^{z_t} v\cos\theta\,\mathrm{d}z\,\mathrm{d}\phi \approx 0. \qquad (12)$$

If we divide the total area $\mathcal{S}$ in to an Atlantic part $\mathcal{S}_A$ and a remainder (Indo–Pacific) part $\mathcal{S}_P$ with characteristic meridional velocities V_A and V_P, respectively, then we have $V_A\mathcal{S}_A + V_P\mathcal{S}_P \approx 0$. Hence, in the upper ocean a near-linear relation exists between the characteristic meridional velocities in the Atlantic and in the Indo–Pacific basins.

We choose the characteristic velocities V_P and V_A as

$$V_A = \max_z |\langle v_A\rangle(\theta_s, z)|; \quad V_P = \max_z |\langle v_P\rangle(\theta_s, z)|, \qquad (13)$$

where the absolute maximum is taken over the top 2000 m. There indeed appears to be a connection between these characteristic velocities (Fig. 9d). A near-linear relation is found between V_A and V_P, again most clearly at larger values of K. Deviations from linearity are likely caused by friction which is relatively large in this model (Dijkstra and Weijer, 2005).

4.3. Processes in the Atlantic

Assuming that the characteristic meridional velocity V_A is set by processes in the Pacific, how can we explain the $K^{1/3}$ scaling of the Atlantic MOC? Let $\Delta\rho_A$ and δ_A be a characteristic meridional density difference and thermocline depth in the Atlantic. In general, when $V_A \sim K^a$, $\psi_A \sim K^b$, $\delta_A \sim K^c$ and $\Delta\rho_A \sim K^d$, the geostrophic and hydrostatic balances require $a = c + d$ and the transport relation $\psi_A \sim V_A\delta_A$ provides the relation $b = a + c$.

To determine an estimate of the exponent c, the depth of the Atlantic thermocline from the model was calculated at 30°W again using eq. (10) with $\eta = 0.5$. The results are plotted for several latitudes in Fig. 10 and are clearly substantially different from those for the Pacific. The thermocline depth (at 30°W) tends to constant values for larger values of K down to 10°S. The thermocline depth increases slightly at more southerly latitudes, probably because of coupling with the flow in the Southern Ocean. From Fig. 10, we may conclude that c is small, though perhaps not zero, when considered over the whole Atlantic.

For the dominant balances in the density equation, we choose a location Q_A (30°W, 50°N) in the North Atlantic just south of the sinking region. Down to 10°S, similar balances in the density equation hold. At the location Q_A, the balances in the density equation for two values of K are plotted in Figs. 11a and b. The curve labeled **check** is again the net residue in the density balance which is about 0.1% of the largest terms in the equation. In the pycnocline region, it appears that many terms contribute

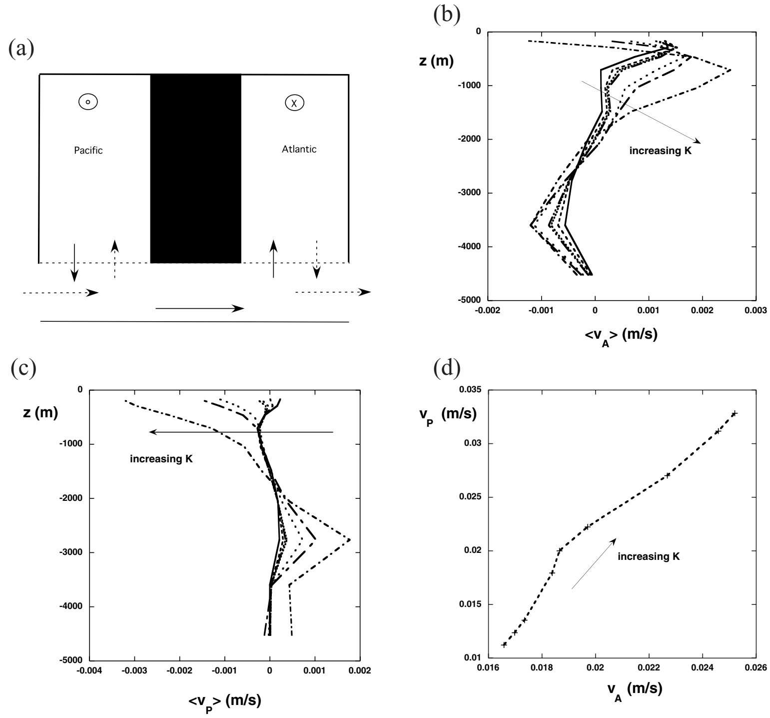

Fig. 9. (a) Sketch of the two-basin situation; surface (deep) currents are indicated by solid (dotted) arrows. (b) Plot of $\langle v_A\rangle(\theta_s, z)$ for several values K where $\theta_s = 35°$S. (c) Plot of $\langle v_P\rangle\ (\theta_s, z)$ for several values K where $\theta_s = 35°$S. The different line styles indicate different values of κ as in Fig. 7a. (d) Relation between V_A and V_P as in (13) for different values of K and $\theta_s = 35°$S.

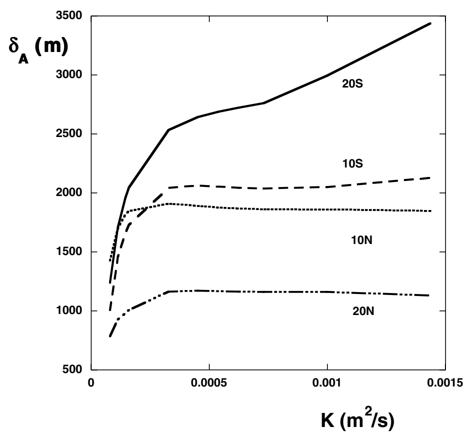

Fig. 10. Dependence of the area mean (bounded by a 20° section in longitude and 10° section in latitude centred around 30°W in the Atlantic) pycnocline depth δ_A in (10, with $\eta = 0.5$) on K.

to the density balance in the North Atlantic and there is no clear advection–diffusion balance as in the Pacific.

In Fig. 12a, the vertical density distribution for several values of K is plotted at Q_A. It is seen that the pycnocline depth hardly changes with K over the range of K computed. As the ocean model is coupled to an energy balance atmosphere model, the (sub)surface density values may vary with K. The vertically averaged meridional density difference $\Delta\rho$ as in eq. (9) is plotted in Fig. 12b for different choices of the southern boundary θ_s. Although there is a sensitivity to the domain boundaries, it is clear that $\Delta\rho$ increases with K. The northern density (Fig. 12a) decreases due to the increase in heat transport, but the southern density decreases even more and hence the north–south density difference increases. There is no nice power-law scaling; a power-law fit using a southern boundary of $\theta_s = 35°$S in the large K range provides a best exponent d of about 0.25.

These results support the following 'ideal' interpretation of the model behaviour. In the Atlantic, the thermocline is advectively controlled certainly down to 10°S and hence its depth does not change with K (i.e. $c \approx 0$). In this case, V_A is totally determined by processes in the Pacific, and $V_A \sim V_P \sim K^{1/3}$ through the southern connection, which gives $a = 1/3$. Through the transport relation, it also implies $b = a$, which explains the $\psi_A \sim K^{1/3}$ relation found in the model. Finally, the geostrophic and hydrostatic balance imply that $d \approx 1/3$, and this is established through the fact that the upper layer density can change due to interaction with the overlying atmosphere. In the model here, the exponent c is slightly larger than zero, probably because of changes in the southern thermocline, which are dependent on K, and the exponent d is consequently slightly smaller than $1/3$.

5. Summary and Discussion

The scaling behaviour of the Atlantic MOC versus changes in K_V has been considered using a global fully-implicit OGCM. Although this model has its deficiencies such as a too simple representation of mixing processes (Dijkstra and Weijer, 2005), it is possible to efficiently compute steady-states versus K_V.

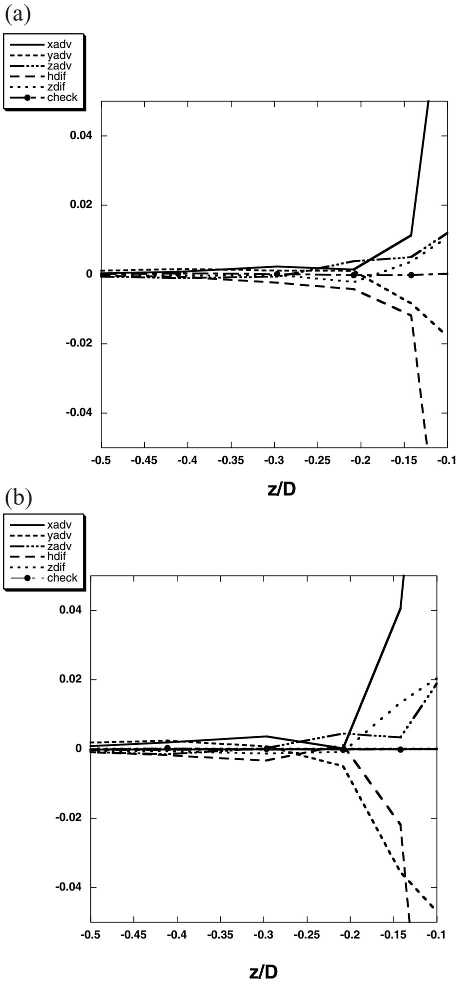

Fig. 11. Terms in the density equation for two values of K in the North Atlantic at the location Q_A (50°N, 30°W) over a range of z/D with $D = 5000$ m. The different terms are indicated on the y-axis, with **xadv**: zonal advection, **yadv**: meridional advection, **zadv**: vertical advection, **hdif**: horizontal diffusion, **zdif**: vertical diffusion and **check** is the net residue in the density equation. (a) $K = 8.0 \times 10^{-5}$ m^{2}s^{-1}. (b) $K = 1.5 \times 10^{-4}$ m^{2}s^{-1}.

Instead of having only a handful of solutions (which may not even be in equilibrium) as in most other studies, we base the scaling relation on relatively many exact steady solutions.

Under restoring conditions, there is a clear $K_V^{1/3}$ power-law dependence of the strength of the Atlantic MOC ψ_A and a $K_V^{2/3}$ power-law dependence of the strength of the Pacific MOC ψ_P. By analysing the different terms in the density equation, it appears that the presence of the Pacific basin is essential for the scaling behaviour. While the depth of the Atlantic pycnocline (δ_A) hardly changes with K_V, the depth of Pacific pycnocline (δ_P) is determined by classical (advective/diffusive) scaling. As a consequence, characteristic horizontal velocities V over the global domain scale with $K_V^{1/3}$, the Pacific MOC scales with $K_V^{2/3}(\sim V\delta_P)$ but the Atlantic MOC with $K_V^{1/3}(\sim V\delta_A)$. The fact that the meridional velocities have a similar scaling in the Atlantic and the Pacific but the resulting transport is different, is possible because in the Atlantic, part of the transport can occur below the thermocline. Although still quite speculative, this water may then recirculate before it reaches the North Atlantic and hence it is not contributing to the strength of the MOC.

Compared with the classical theories, the extension here is that the balances determining the horizontal velocities are set by the advective–diffusive balance in the Pacific pycnocline, whereas advective processes determine the pycnocline depth in the Atlantic. This provides a good explanation for the model results, which are supported by the dominant balances in the density equation in both basins near the pycnocline. However, the model here has many deficiencies and a legitimate question therefore is what conclusions can be drawn about (i) the behaviour of global ocean (and climate) models and (ii) the behaviour of the real ocean?

Based on our results here, we can address the issue raised in Levermann and Griesel (2004) that the Gnanadesikan (1999) theory is flawed because their GCM results do not show the predicted scaling behaviour. Although in the Gnanadesikan (1999) model it has been assumed that the surface density is prescribed, and the GCM results in Levermann and Griesel (2004) are under mixed boundary conditions (and so may be a bit beyond the scope of this theory), the results in this paper indicate that indeed the Gnanadesikan (1999) theory cannot explain the scaling of the AMOC. The reason is that the theory (i) lacks the presence of a second basin (here the Pacific) where the pycnocline depth is determined by an advective–diffusive density balance and (ii) does not represent the advectively controlled pycnocline depth in the Atlantic. The classical 2/3 power-law scaling, however, does apply to the global overturning flow and so the Gnanadesikan (1999) theory appears to work for the global overturning circulation.

Whether other ocean or ocean-climate models will display the $K_V^{1/3}$ scaling of the Atlantic MOC is to be seen, and this study hopefully motivates future GCM computations with these models. The results here are consistent with available model results in the literature (Dalan et al., 2005; Furue and Endoh, 2005); when K_V is locally decreased in the Pacific pycnocline, the characteristic horizontal velocity decreases and hence the Atlantic MOC also. Note that in the model here, values of K_V are relatively large, with a minimum value of 8.0×10^{-5} m^{2}s^{-1}, and for smaller K_V, wind stress may be controlling the strength of the global MOC even more. In this model, decreasing K_V gives an unrealistically small value of the overturning due to deficiencies discusses at length in Dijkstra and Weijer (2005).

In the real ocean, the mixing field is highly variable, both spatially and temporally, and it is impossible to conclude anything on scaling relations based on the model results here. What remains as bottom line of this paper is that the processes

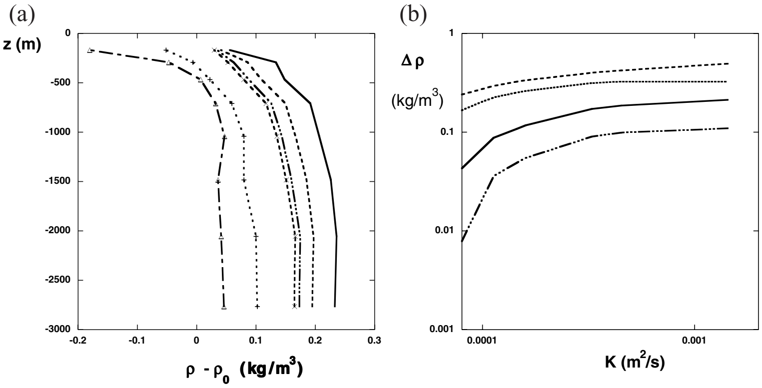

Fig. 12. (a) Vertical profiles of $\rho - \rho_0$ in the North Atlantic at the location Q_A at (30°W, 50°N) for different values of $K = \kappa\, K_V^0$ with: $\kappa = 1.0$ (solid); $\kappa = 1.41$ (dashed); $\kappa = 1.82$ (dashed-dotted); $\kappa = 2.0$ (dashed-crosses); $\kappa = 4.1$ (dotted-plusses) and $\kappa = 5.6$ (dashed-dotted-triangles). (b) Vertically averaged meridional density difference $\Delta\rho$ as in eq. (9), with $z_b = -1000$ m, $z_t = -20$ m, for four different choices of θ_n and θ_s with: $\theta_n = 60°$N; $\theta_s = 35°$S (drawn); $\theta_n = 60°$N; $\theta_s = 10°$S (dotted); $\theta_n = 60°$N, $\theta_s = 10°$N (drawn); $\theta_n = 60°$N and $\theta_s = 20°$N (dashed-dotted).

setting the pycnocline in the Pacific may be crucially important for the amplitude of the Atlantic overturning; this needs exploration through more sophisticated models.

6. Acknowledgments

All computations were done on the SGI Origin 3800 computer at SARA Amsterdam. Use of these computing facilities was sponsored by the National Computing Facilities Foundation (N.C.F.) under the project SG192 with financial support from the Netherlands Organization for Scientific Research (N.W.O.). The author thanks Olwijn Leeuwenburgh (IMAU) and both anonymous referees for very useful comments on the earlier versions of this paper.

References

Bryan, F. 1987. Parameter sensivity of primitive equation ocean general circulation models. *J. Phys. Oceanogr.* **17**, 970–985.

Bryan, K. and Cox, M. D. 1967. A numerical investigation of the oceanic general circulation. *Tellus* **19**, 54–80.

Bryan, K. and Lewis, L. J. 1979. A water mass model of the world ocean. *J. Geophys. Res.* **84**, 2503–2517.

Colin de Verdière, A. 1988. Buoyancy driven planetary flows. *J. Mar. Res.* **46**, 215–265.

Dalan, F., Stone, P., Kamenkovich, I. and Scott, J. 2005. Sensitivity of the ocean's climate to diapycnal diffusivity in an EMIC. Part I: equilibrium state. *J. Climate* **18**, 2460–2481.

Dijkstra, H. A. 2005. *Non-linear Physical Oceanography: A Dynamical Systems Approach to the Large Scale Ocean Circulation and El Niño*, 2nd Revised and Enlarged edition. Springer, New York, 532 pp.

Dijkstra, H. A. and Weijer, W. 2005. Stability of the global ocean circulation: basic bifurcation diagrams. *J. Phys. Oceanogr.* **35**, 933–948.

Dijkstra, H. A., Öksüzöglu, H., Wubs, F. W. and Botta, E. F. F. 2001. A fully implicit model of the three-dimensional thermohaline ocean circulation. *J. Comput. Phys.* **173**, 685–715.

England, M. H. 1993. Representing the global-scale water masses in ocean general circulations models. *J. Phys. Oceanogr.* **23**, 1523–1552.

Furue, R. and Endoh, M. 2005. Effects of the Pacific diapycnal mixing and wind stress on the global and Pacific meridional overturning. *J. Phys. Oceanogr.* **35**, 1876–1890.

Gnanadesikan, A. 1999. A simple predictive model of the structure of the oceanic pycnocline. *Science* **283**, 2077–2081.

Hu, D. 1996. On the sensitivity of thermocline depth and meridional heat transport to vertical diffusivity in OGCMs. *J. Phys. Oceanogr.* **26**, 1480–1494.

Keller, H. B. 1977. Numerical solution of bifurcation and non-linear eigenvalue problems. In *Applications of Bifurcation Theory* (ed. P. H. Rabinowitz). Academic Press, New York, USA.

Klinger, B. A., Drijfhout, S., Marotzke, J. and Scott, J. R. 2003. Sensitivity of basinwide meridional overturning to diapycnal difffusion and remote wind forcing in an idealized Atllantic-Southern Ocean geometry. *J. Phys. Oceanogr.* **33**, 249–266.

Levermann, A. and Griesel, A. 2004. Solution of a model for the oceanic pycnocline depth: scaling of overturning strength and pressure difference. *Geophys. Res. Lett.* **31**, L17302, doi:10.1029/2004GLO20678.

Levitus, S. 1994. World Ocean Atlas 1994, Volume 4: Temperature. *NOAA/NESDIS E, US Department of Commerce, Washington DC*. **OC21**, 1–117.

Lineikin, P. S. 1955. On the determination of the thickness of the baroclinic layer in the sea. *Dokl. Akad. Nauk USSR* **101**, 461–464.

Lucas, M. A., Hirschi, J. and Marotzke, J. 2006. The scaling of the meridional overturning with the meridional temperature gradient in idealised general circulation models. *Ocean Modelling* **13**, 306–318.

Marotzke, J. and Scott, J. R. 1997. Boundary mixing and the dynamics of the three-dimensional thermohaline circulation. *J. Phys. Oceanogr.* **27**, 1713–1728.

Olbers, D. 1998. Comments on 'On the obscurantist physics of form drag in theorizing about the Circumpolar Current'. *J. Phys. Oceanogr.* **28**, 1647–1654.

Park, Y.-G. and Bryan, K. 2000. Comparison of thermally driven circulations from a depth-coordinate model and an isopycnal-layer model. Part I: Scaling-law sensitivity to vertical diffusivity. *J. Phys. Oceanogr.* **30**, 590–605.

Park, Y.-G. and, Bryan, K. 2001. Comparison of thermally driven circulations from a depth-coordinate model and an isopycnal-layer model. Part II: The difference and structure of the circulations. *J. Phys. Oceanogr.* **31**, 2612–2624.

Rahmstorf, S. 1996. On the freshwater forcing and transport of the Atlantic thermohaline circulation. *Clim. Dyn.* **12**, 799–811.

Rahmstorf, S. 2000. The thermohaline circulation: a system with dangerous thresholds? *Climatic Change* **46**, 247–256.

Robinson, A. and Stommel, H. 1959. The oceanic thermocline and the associated thermohaline circulation. *Tellus* **3**, 295–308.

Trenberth, K. E., Olson, J. G. and Large, W. G. 1989. A global ocean wind stress climatology based on ECMWF analyses. Technical report, National Center for Atmospheric Research, Boulder, CO, USA.

Warren, B. A., LaCasce, J. H. and Robbins, P. E. 1997. On the obscurantist physics of form drag in theorizing about the Circumpolar Current. *J. Phys. Oceanogr.* **26**, 2297–2301.

Weijer, W., Dijkstra, H. A., Oksuzoglu, H., Wubs, F. W. and De Niet, A. C. 2003. A fully-implicit model of the global ocean circulation. *J. Comp. Phys.* **192**, 452–470.

Welander, P. 1986. Thermohaline effects in the ocean circulation and related simple models. In *Large-Scale Transport Processes in Oceans and Atmosphere* (eds. J. Willebrand, and D. L. T. Anderson) D. Reidel, 163–200.